

Available online at www.sciencedirect.com

ScienceDirect

journal homepage: www.elsevier.com/locate/he

Proton exchange membrane fuel cell failure mode early diagnosis with wavelet analysis of electrochemical noise

M.A. Rubio ^{a,*}, K. Bethune ^b, A. Urquia ^a, J. St-Pierre ^b^a Dept. Informática y Automática, Universidad Nacional de Educación a Distancia (UNED), 28040 Madrid, Spain^b Hawaii Natural Energy Institute, University of Hawaii, Manoa, Honolulu, HI 96822, USA

ARTICLE INFO

Article history:

Received 19 April 2016

Received in revised form

26 May 2016

Accepted 30 May 2016

Available online 21 June 2016

Keywords:

Electrochemical noise

Electrochemical impedance

spectroscopy

Diagnosis

Wavelet transform

PEM fuel cell

ABSTRACT

A diagnostic method for the performance degradation of low temperature proton exchange membrane fuel cells is proposed. The method is based on the analysis of the cell electrochemical noise. Experimental noise data were collected for a range of air relative humidities and stoichiometries including conditions leading to water flooding, membrane dehydration and air starvation failure modes. Data were converted with a Fourier transform (frequency window averaging of the amplitude) and a wavelet transform (coefficients standard deviation). Data were compared to impedance spectroscopy results. The method based on the wavelet transform was more sensitive. Cell states labeled by their air relative humidity and stoichiometry were correctly identified using a brute force algorithm by minimizing the Chebyshev distance between the actual and the calculated states. Independent and uniformly distributed random variations were added to experimental wavelet coefficients' standard deviations to define the calculated states.

© 2016 Hydrogen Energy Publications LLC. Published by Elsevier Ltd. All rights reserved.

Introduction

Proton exchange membrane fuel cells (PEMFCs) are considered as an option to power a range of devices due to advantages, such as high efficiency, quiet operation and environmental friendliness, if fed with hydrogen generated from solar energy. These devices are subject to failure modes requiring diagnostic equipment for identification. Flooding of flow field channels by liquid water has been studied using transparent fuel cell designs [1]. Local fuel starvation is detected by segmented cell designs for current and voltage distributions [2]. However, these methods are invasive and

affect the system being measured. The transparent fuel cell wall is a thermal insulator as opposed to the heat conductive carbon bipolar plate [1]. A significant change in surface properties is also introduced, which affects water management. As for segmented cell measurements, the insulator separating the segments translates into a decrease in the active area for electronic conduction through the bipolar plate. Furthermore, the use of shunt resistors to measure the current distribution induces changes absent during normal fuel cell operation [3]. As a result, efforts have been devoted to the development of less invasive measurement methods, such as neutron imaging to measure the water distribution [1] and magnetic field sensors external to the fuel cell to measure current

* Corresponding author.

E-mail address: marubio@dia.uned.es (M.A. Rubio).<http://dx.doi.org/10.1016/j.ijhydene.2016.05.292>

0360-3199/© 2016 Hydrogen Energy Publications LLC. Published by Elsevier Ltd. All rights reserved.

distributions [4]. However, these methods still require significant equipment and expenses that cannot be incorporated into actual fuel cell system operations.

A more elegant, non-invasive approach is available by listening to the electrochemical device, recording and analyzing the noise generated. Such an approach has been investigated for corrosion processes [5–7], batteries [8–10] and coatings [11–13]. Only a few reports discuss applications to fuel cells [14–17]. However, in the first report, the electrochemical noise was monitored with a biofuel cell [14], which is not relevant to the present PEMFC discussion. In other studies, only a single failure mode is considered [15,16] by varying the relative humidity of the reactant streams. This is an unrealistic situation for the commercial introduction of fuel cells as several failure modes were identified. As for the last report, the authors proposed 5 different methodologies to analyze fuel cell noise [17]. However, the proposed methods were not applied to fuel cell data, and therefore, their effectiveness is unknown. More recent efforts have focused on the use of the wavelet transform and calculated wavelet coefficients [18–21]. However, the full potential of this approach has not been fully explored in view of the number of diagnostic parameters that can be derived from the wavelet coefficients (for instance the average, standard deviation and total energy).

Other approaches based on noise measurements have been proposed. Acoustic emissions generated during material deformation were demonstrated for membrane dehydration [22,23]. Fuel cell impedance noise at low frequencies was correlated with water drop formation [24]. Magnetic field noise surrounding a fuel cell during operation was linked to flow field channel flooding, membrane pinholes and hydrogen contaminated with acetone [25]. All of these examples suffer from at least one of the following issues: the noise is induced with the use of an excitation signal (impedance measurements), methods need to be ascertained for fuel cell failure modes other than those originally considered, equipment that is not expected to be part of a fuel cell system is needed, or a clear distinction between different failure modes (unique signatures) was not proven. Two noise amplification techniques were also suggested: superimposed pressure oscillations [26,27] and pseudo-random binary sequences in the current [28]. However, in both cases, additional equipment is required, which negatively impacts system simplification for reduced cost and improved robustness.

The development of an early detection and identification strategy for PEMFC failure modes during operation is the focus of the present study. The fuel cell voltage noise is collected and analyzed because the fuel cell system is expected to include electrical variable measurement equipment, such as a cell voltage monitoring system [29]. The air stoichiometry and relative humidity were varied to emphasize ionomer dehydration, flooding and starvation failure modes. Fourier and wavelet transform analyses of the measured noise and electrochemical impedance spectroscopy (EIS) data were compared to determine the best strategy in terms of sensitivity, real time analysis and existence of unique signatures. Wavelet transform (WT) and short-time Fourier transform (STFT) were suited for failure detection and diagnosis in real time. These two methods are compared in Refs. [30,31]. It was

concluded that STFT provides faster signal processing, but WT provides a higher-quality analysis at the expense of a greater computational cost. It is emphasized that the noise analyses were completed off-line in this report to demonstrate feasibility. The real-time implementation of the method for an enlarged set of failure modes is left to a subsequent report.

Experimental

Fuel cell and test station

The experimental work was performed at the Hawaii Sustainable Energy Research Facility (HiSERF) at the Hawaii Natural Energy Institute. Fuel Cell Technologies 50 cm² single cell hardware with a double serpentine anode and triple serpentine cathode flow fields were utilized. Membrane/electrode assemblies (MEA) were produced by General Motors Research and consisted of a Dupont Nafion NRE211 membrane and electrodes with 0.05 and 0.4 mg cm^{−2} platinum loadings on the anode and cathode, respectively, using Vulcan carbon as the support. The electrode ionomer was Dupont Nafion perfluorosulfonic acid dispersion D2020, and the diffusion media utilized was MRC105 from 3M. Virgin PTFE gaskets were used for sealing and as shims to achieve ~ 20% compression of the diffusion media.

All experiments were conducted using a fuel cell test station originally constructed by UTC Power (formerly International Fuel Cells). The station uses two National Instruments SCXI data acquisition chassis, a LabVIEW based GUI developed in-house and a scripting system for station control. The fuel cell was operating in counter-flow mode with the cell temperature control in the cathode flow field (end plate cartridge heaters). The gases were humidified using an Arbin DPHS-D10 humidifier with heated gas transfer lines. The cell pressure was controlled at the outlet of the fuel cell.

Test conditions and sequence

For all experiments, several cell operating conditions were held constant while varying the cathode stoichiometric air flow and the cathode humidification levels, i.e., air/H₂, 80 °C cell temperature, 150 kPa absolute outlet pressure, 1.5 anode stoichiometric hydrogen flows, 75% anode relative humidity, and 800 mA cm^{−2} current density. Two separate experimental sequences varying the cathode relative humidity and stoichiometry were used during the noise measurements. In the first experimental sequence, the cathode stoichiometry was swept and the values of the cathode relative humidity were fixed. The cathode stoichiometry was varied from 2 down to 0.9 using steps of 0.1. The fixed relative humidity values were 50, 75, 100, and 125%. As the humidifier reaches steady state much sooner when changing the flow as opposed to changing the dew-point temperature, each step during the stoichiometry sweep was held to 300 s. For the second experimental sequence, the cathode relative humidity was swept while the cathode stoichiometry was fixed. The values of the relative humidity were varied between 50 and 130% using steps of 10%. The fixed value of the stoichiometry was varied from 2 to 1.2 using steps of 0.2. As the humidifier takes longer to stabilize

following dew point temperature changes, the length of each step was extended to 30–45 min with experimental data only recorded during the last 300 s. The results were similar for the equivalent experimental points of the two experimental sequences for noise measurements (~ 3 mV standard deviation). EIS experiments were performed on a subset of the noise conditions limited to a 4×4 matrix where the cathode relative humidity was set at 50, 75, 100, and 125% and the cathode stoichiometry was set at 2, 1.8, 1.6, and 1.4.

Impedance spectroscopy

EIS scans were obtained using a Solartron 1260 Impedance/gain-phase analyzer interfaced with the test station (Transistor Devices Inc. RBL488 50-1000-4000) load bank using ZPlot (Scribner Associates) software. A low-inductance custom Ni–Cr current shunt was used to measure the current perturbation, and the fuel cell voltage was measured with pins inserted in the bipolar plates. Stanford Research SR560 low noise preamplifiers were used to condition the fuel cell voltage and the current measurements prior to being fed back to the Solartron 1260. The frequency range tested was 0.1 Hz–10 kHz with 10 frequencies/decade using an AC current perturbation amplitude of 0.75 A.

Electrochemical noise measurements

A National Instruments (NI) PCIe-6341 PCI express card was used for recording the fuel cell voltage for noise analysis. The NI PCIe-6341 is a multi-function data acquisition card that has a 16-bit resolution and a sampling rate up to 500 kHz. The ± 1 V input gain range was used resulting in a resolution of ± 30.5 μ V at 16 bits. The resolution of the NI PCIe-6341 was improved with an oversampling and averaging scheme. The signal was sampled at 128 kHz and averaged to 2 kHz, which improved the resolution by 3 bits from ± 30.5 μ V to ± 3.8 μ V. A higher resolution, 24-bit NI 9239 analog input module was also evaluated and produced nearly identical results at 2 kHz. The NI PCIe-6341 was selected for the noise measurements and subsequent Fourier and wavelet transform analyses as this hardware was already integral to the test station.

The measured signal, $v(t)$, is the superposition of the quasi-stationary cell voltage, v_{st} , an electrochemical noise signal, $u_{ec}(t)$, and other external (to the cell) noise signals, $u_e(t)$ as is shown in Eq. (1).

$$v(t) = v_{st} + u_{ec}(t) + u_e(t) \quad (1)$$

The electrochemical noise is representative of the fuel cell internal behavior and is, thus, of interest for the purpose of fuel cell diagnosis. The main contribution to the external noise is the instrumental noise generated by the measurement equipment, power sources, and electromagnetic coupling of the electrical conductors. The external and instrumental noise was estimated in Ref. [10] by measuring the open-circuit voltage of the fuel cell in a frequency range below 20 Hz, and in Ref. [12] the contribution of the external and instrumental noise was less than the contribution of the electrochemical noise. For the measurement setup described

previously, a shunt resistor was connected in series with the cell, and the voltage noise signals were measured in the shunt resistor and in the fuel cell simultaneously at a sample rate of 10 kHz to distinguish the instrumental from the electrochemical noise. It is assumed that the noise signal measured in the shunt resistance is primarily due to instrumental noise. As shown in Fig. 1, which compares the power spectrum (discussed in subsequent sections) of the noise measured in the fuel cell and in the shunt resistor, a convergence occurs at approximately 200 Hz. This observation implies that above 200 Hz the noise signal is primarily instrumental noise, and thus, according to the Nyquist theorem, sample rates greater than 400 Hz would not provide any additional information. However, as the ohmic resistance in fuel cells with active areas on the order of 50 cm² is typically measured at 1 kHz [32], 2 kHz (2×1 kHz) was selected as the final sampling rate to be used throughout the experiments as this frequency covered the experimentally determined electrochemical and instrumental transition frequency of 200 Hz and the frequency typically used for ohmic resistance measurements.

Electrochemical noise analyses

The Matlab function `fft()` (fast Fourier transform algorithm) [33] was used to compute the short-time discrete Fourier transform (STFT) and to perform the discrete Fourier transform analyses with frequency window averaging.

The wavelet toolbox of Matlab was used to perform the wavelet transform analyses. Noise data were recorded in every experiment for 300 s. However, only the data recorded during the last 50 s were considered in the analyses. This 50 s time-window was found to be large enough to estimate the cell state, while keeping the computational load as low as possible.

Results and discussion

Data analysis

Electrochemical noise signals separated into temporal windows were processed offline, either using the short-time

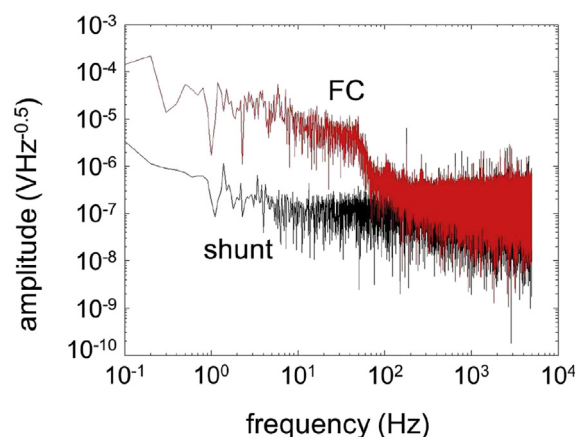


Fig. 1 – Spectrum amplitude of the noise measured in the shunt resistor and the fuel cell sampled at 10 kHz.

discrete Fourier transform (STFT) or a wavelet transform (WT) [34,35], with the objective to identify fingerprints associated with specific fuel cell states including failure modes. The STFT has been in use for steady state signal analysis for a time-window and is considered here as a comparative baseline. In contrast, the wavelet transform is a more recently and specifically developed approach tailored to dynamic signals. The beneficial properties of the wavelet transform for the detection of changes in transient signals are in part attributable to a limited width of the wavelets in the time domain, whereas it is a time-window for the STFT. Two frequency domain analysis methods are examined for the discrete Fourier transformed data, whereas a single method is considered for the wavelet transform case. The transform based analysis methods are compared to impedance spectroscopy because it is a well-known electrochemical diagnostic technique [36], even if additional equipment and an applied signal are required.

Fourier transform

The first method consisted of calculating the short-time Fourier transform (STFT single frequency window) to obtain the spectrum:

$$X(k) = \sum_{n=0}^{N-1} x(n) e^{-j2\pi kn/N} \quad k = 0, 1, 2, \dots, N-1 \quad (2)$$

where $X(k)$ are the STFT coefficients of the N -length discrete signal $x(n)$. The discrete frequencies are related to k , $f(k) = k/(n\Delta t)$, where Δt represents the period of the data sampling rate. The absolute values of complex STFT coefficients, $|X(k)|$, define the amplitude spectrum.

The spectrum is subsequently analyzed by fitting the linear decay slope to $f^{-\alpha}$ (Fig. 2), where f is the frequency and α is a positive rational coefficient [15,37,38]. It was observed that the fitted value of α depends strongly on decisions made during the fit process, i.e., the selection of the data set used to

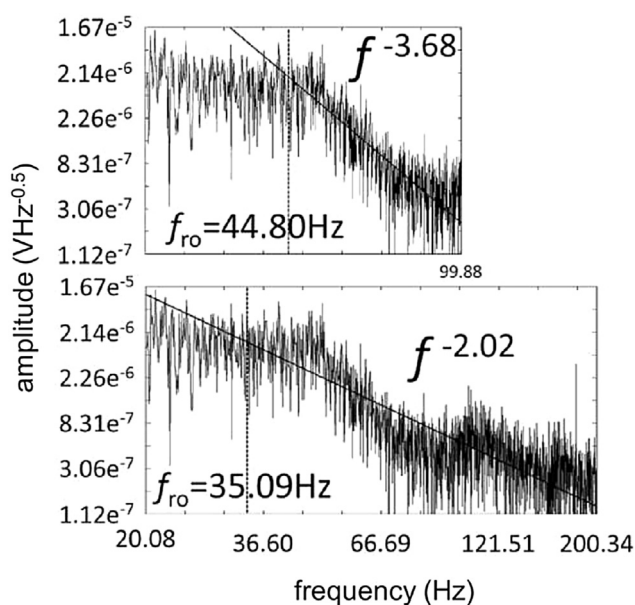


Fig. 2 – Linear fit of spectra calculated from the same noise measurements for different frequency windows and roll-off frequencies f_{ro} .

characterize the low-frequency plateau and the selection of the roll-off frequency. For instance, α increases by 82% with an increase in the roll-off frequency from 35.09 Hz to 44.80 Hz.

The second method for data analysis, which was previously used in Ref. [9] to detect battery overcharge, consists of calculating the STFT as in the first method, defining the frequency bands and characterizing the phenomena in these different bands. In this manner, the number of parameters is increased in comparison to the first method, facilitating the identification of many phenomena. The 0.2–100 Hz range has been divided into five frequency bands: 0.2–1 Hz, 1–2.8 Hz, 2.8–11 Hz, 11–35 Hz and 35–100 Hz. The average value of the spectrum B_m in each band is calculated from Eq. (3).

$$B_m = \frac{\sum_{k=a}^b X(k)}{M} \quad (3)$$

where a and b are the lowest and highest values of the frequencies in the m -th band, and M is the total number of frequencies calculated in this band.

This method allows searching each studied phenomenon in its characteristic frequency band. Conversely, it is possible to choose the frequency bands on the basis of the time scales of the studied elementary processes [1]. To facilitate method comparison, the frequency bands are centered at the frequencies used in the WT analysis.

The complete spectra obtained for 50% and 125% relative humidity and the selected frequency bands are shown in Fig. 3. The cathode stoichiometry is equal to 2 in both cases. The two spectra were observed to be significantly different within the 1–2.8 Hz, 2.8–11 Hz and 11–35 Hz bands.

Wavelet transform

The third method for data analysis is based on the use of a wavelet transform [34,35]. The signal, rather than being decomposed into a series of sinusoidal waves of different frequencies (FT), is separated into wavelets that are a scaled

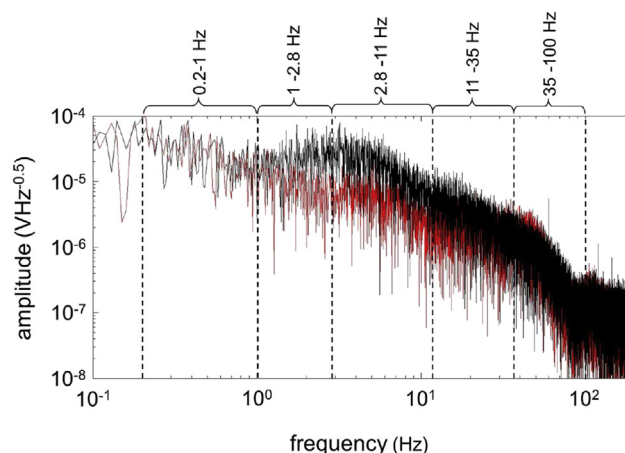


Fig. 3 – Spectra amplitude corresponding to two cathode relative humidity values: 0.5 (red) and 1.25 (black). The cathode stoichiometry is equal to 2 in both cases. (For interpretation of the references to colour in this figure legend, the reader is referred to the web version of this article.)

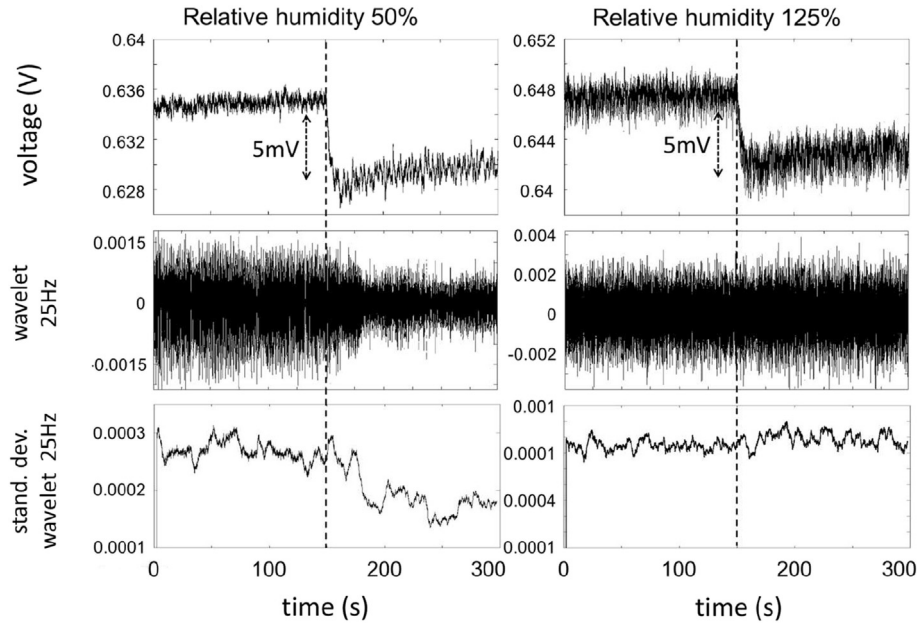


Fig. 4 – Cell voltage and corresponding 25 Hz wavelet transform coefficient and associated standard deviation. The cathode stoichiometry is changed from 1.7 to 1.6 at a time equal to 150 s for two values of the cathode relative humidity, 50 and 125%.

and shifted version of the mother wavelet. The wavelet transform is particularly suitable for the analysis of signals with discontinuities or rapid changes and the temporal localization of these features because the wavelets are irregular in shape and finite across the time domain. Therefore, signal analysis in real time is enabled. This feature is illustrated in Fig. 4 with transitions in cathode stoichiometry for two different values of relative humidity. The voltage drop was approximately 5 mV for both transitions (upper part of the figure). The signal is noisier for the 125% relative humidity case due to the presence of a larger number of liquid water drops and the stochastic nature of their growth and detachment [24]. Transitions also lead to a smaller cell voltage due to increased mass transfer losses for lower air stoichiometries [39]. The stoichiometry transitions occur at a time equal to 150 s. Differences between the 25 Hz wavelet coefficients (described in more detail below) are shown as an example in the lower part of the figure. Wavelet coefficients hardly vary during the transition. However, the effect on the wavelet coefficient standard deviation is significantly greater for the 50% relative humidity case. In comparison, for the 125% relative humidity case, the wavelet coefficient standard deviation was not noticeably affected. Additionally, the standard deviation change is perceptible after the stoichiometry transition within 50 s. In view of its greater sensitivity, the standard deviation of the wavelet coefficient is used rather than the wavelet coefficient itself.

The use of several wavelet families was evaluated, including Haar, Daubechies, Mexican Hat and Gauss. Significant differences were observed when analyzing high frequencies (>200 Hz). However, results for all the wavelet families were similar in the frequency range of interest for this study. The Gauss type 4 wavelet transform was selected

for demonstration purposes. The family of Gaussian functions is defined by Eq. (4).

$$\psi_{\text{Gauss}}(t, n) = C_n \frac{d^n}{dt^n} (e^{-t^2}) \quad (4)$$

where C_n is such that the square norm of $\psi_{\text{Gauss}}(t, n)=1$. The type 4 is obtained by taking the 4th derivative of ψ_{Gauss} and is illustrated in Fig. 5. The width of these wavelet functions can be infinite, and the functions are symmetric.

The continuous wavelet transform (CWT) is used to calculate the wavelet coefficients W . The CWT of a function $f(t)$ is represented by Eq. (5) [34], where a is the scale factor, b is the translation factor and ψ^* denotes the complex conjugate of the wavelet function.

$$W(a, b, f(t), \psi(t)) = \int_{-\infty}^{\infty} f(t) \frac{1}{\sqrt{a}} \psi^* \left(\frac{t-b}{a} \right) dt \quad (5)$$

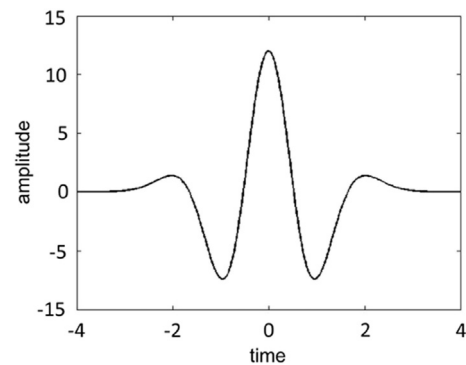


Fig. 5 – Gaussian derivative type 4 wavelet.

The noise sensitivity at a specific frequency is estimated by calculating the standard deviation of the wavelet coefficient associated with that frequency [40]. The following frequencies, f_a , are considered: 50, 25, 5, 1.667 and 0.5 Hz. The selected frequencies are equally separated along a logarithmic scale. The scale factor coefficients for these frequencies are calculated using Eq. (6), where f_c is the center frequency of the wavelet. The value of f_c is 0.5 for a Gauss type 4 wavelet [40], and the sampling period T_s is $5 \cdot 10^{-4}$ s. The calculated values of the scale factor coefficient a are 20, 40, 200, 600, and 2000, as calculated from Eq. (6).

$$a = \frac{f_c}{f_a T_s} \quad (6)$$

The standard deviation of the m -th wavelet coefficient, $\sigma_w(m, N)$, is calculated as shown in Eq. (7). The average value of the m -th wavelet coefficient on N time instants, which is represented as $\bar{W}(m, N)$, is calculated from Eq. (8). In this case study, the value of N is 100 000, which corresponds to the wavelet coefficients derived from 50 s of data measurements sampled at 2 kHz.

$$\sigma_w(m, N) = \sqrt{\frac{\sum_{n=1}^N (W(m, n) - \bar{W}(m, N))^2}{N - 1}} \quad (7)$$

$$\bar{W}(m, N) = \frac{1}{N} \sum_{n=1}^N W(m, n) \quad (8)$$

Electrochemical impedance spectroscopy

EIS, which is the final analysis method, was added as a reference considering its popularity with electrochemists [36]. Sinusoidal signals of different frequencies are superimposed on either the cell voltage or the current, and the corresponding responses, which are the cell current or voltage, are measured. The impedance, which is the ratio of the cell voltage to the cell current, is subsequently calculated and is most frequently depicted as the negative imaginary impedance and is a function of the real impedance (Nyquist representation). This method allows a separation of the different fuel cell processes because they occur at different characteristic frequencies. Exemplary results are shown in Fig. 6. Two main semi-circular

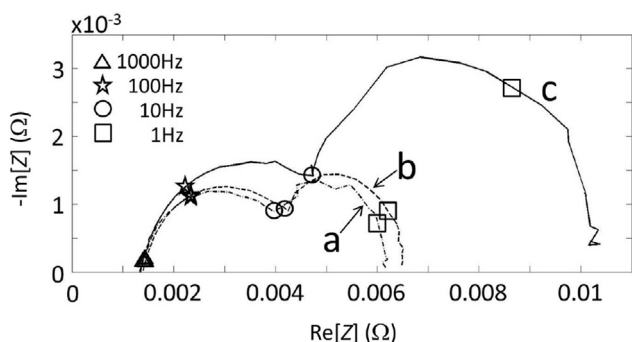


Fig. 6 – EIS Nyquist plots for three experimental conditions: (a) cathode stoichiometry of 1.8 and 100% relative humidity; (b) cathode stoichiometry of 1.8 and 50% relative humidity; and (c) cathode stoichiometry of 1.4 and 100% relative humidity.

loops are observed and are ascribed to the oxygen reduction reaction (~ 10 –1000 Hz) and the mass transfer (<10 Hz) [41]. A faint shoulder is sometimes also noted at high frequencies and is attributed to the hydrogen oxidation reaction [41]. The effects of a decrease in air stoichiometry and an increase in air relative humidity are also shown, which results, in both cases, in an increase in the mass transfer loop and a relatively smaller increase in the oxygen reduction reaction loop. These results are consistent with prior reports [42,43].

Experimental results

A detection method that is able to rapidly detect fuel cell failure modes and avoid irreversible damage (prolonged exposure to air starvation for example [44]) is the focus of the present study. Therefore, experimental data points leading to a significant voltage drop over the nominal value were ignored. Specifically, data corresponding to air stoichiometries below 1.4 were not considered (Fig. 6). Only membrane dehydration and electrode flooding aspects (air relative humidity change) are explored here, leaving air starvation to a subsequent report.

Fuel cell characterization

An example of an air stoichiometry sweep is shown in Fig. 7. As the stoichiometry decreases from 2 to 1.15, the noise level increases. This situation is similar to the results depicted in Fig. 4. However, below a 1.15 stoichiometry value, the trend is reversed. This is tentatively explained by the substantial amount of local heat generated at these low cell voltages (the difference with the thermoneutral voltage is significantly greater [45]) and the appearance of hydrogen evolution [2], which, respectively, favor water evaporation and a decrease in the proportion of the current assigned to oxygen being reduced to water. Finally, at the end of each constant air stoichiometry stage, the cell voltage was relatively stable supporting the use of the last 50 s of data for noise analyses. The air relative humidity sweep is illustrated in Fig. 8. The noise level increases with an increase in the air relative humidity. The observation is ascribed to the presence of a larger proportion of liquid water droplets and films impeding oxygen transport and their stochastic removal [24] from the catalyst surface, the gas diffusion electrode and the flow field channels. The cell voltage was, again, relatively stable at the end of each air relative humidity stage.

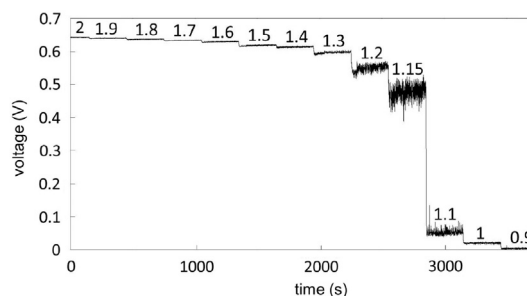


Fig. 7 – Cell voltage obtained by sweeping the cathode stoichiometry value from 2 down to 0.9. The cathode relative humidity was 50%.

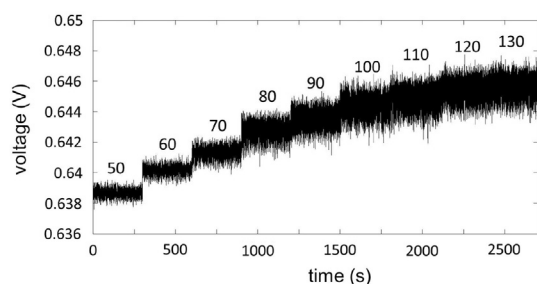


Fig. 8 – Cell voltage obtained by sweeping the relative humidity of the cathode value from 50% up to 130%. The cathode stoichiometry was 2.

Electrochemical noise analyses

Analyses of the fuel cell noise data are summarized in Figs. 9–10. The standard deviations of the wavelet coefficients are

compared with the EIS measurements in Fig. 9 for the same operating conditions and frequencies. The standard deviation of the wavelet coefficients is represented in the left column of Fig. 9. For the two higher frequencies (50 and 25 Hz), the standard deviation of the wavelet coefficients and, consequently, the noise amplitude were observed to increase with the relative humidity. For the two lower frequencies (1.6 and 0.5 Hz), increasing the stoichiometry reduced the wavelet coefficient standard deviation. The results for 5 Hz are intermediate, showing variations in the standard deviation of the wavelet coefficient that are a function of both the air stoichiometry and the relative humidity. The overall magnitude and pattern of these variations in the standard deviation of the wavelet coefficients define a signature that may be used to identify the cell state as discussed in the next section.

The cell impedance measured using the EIS is shown in the three last columns of Fig. 9. The frequency range of 0.5–50 Hz is representative of both oxygen reduction kinetics and oxygen mass transfer (Fig. 6) [46], which is consistent with

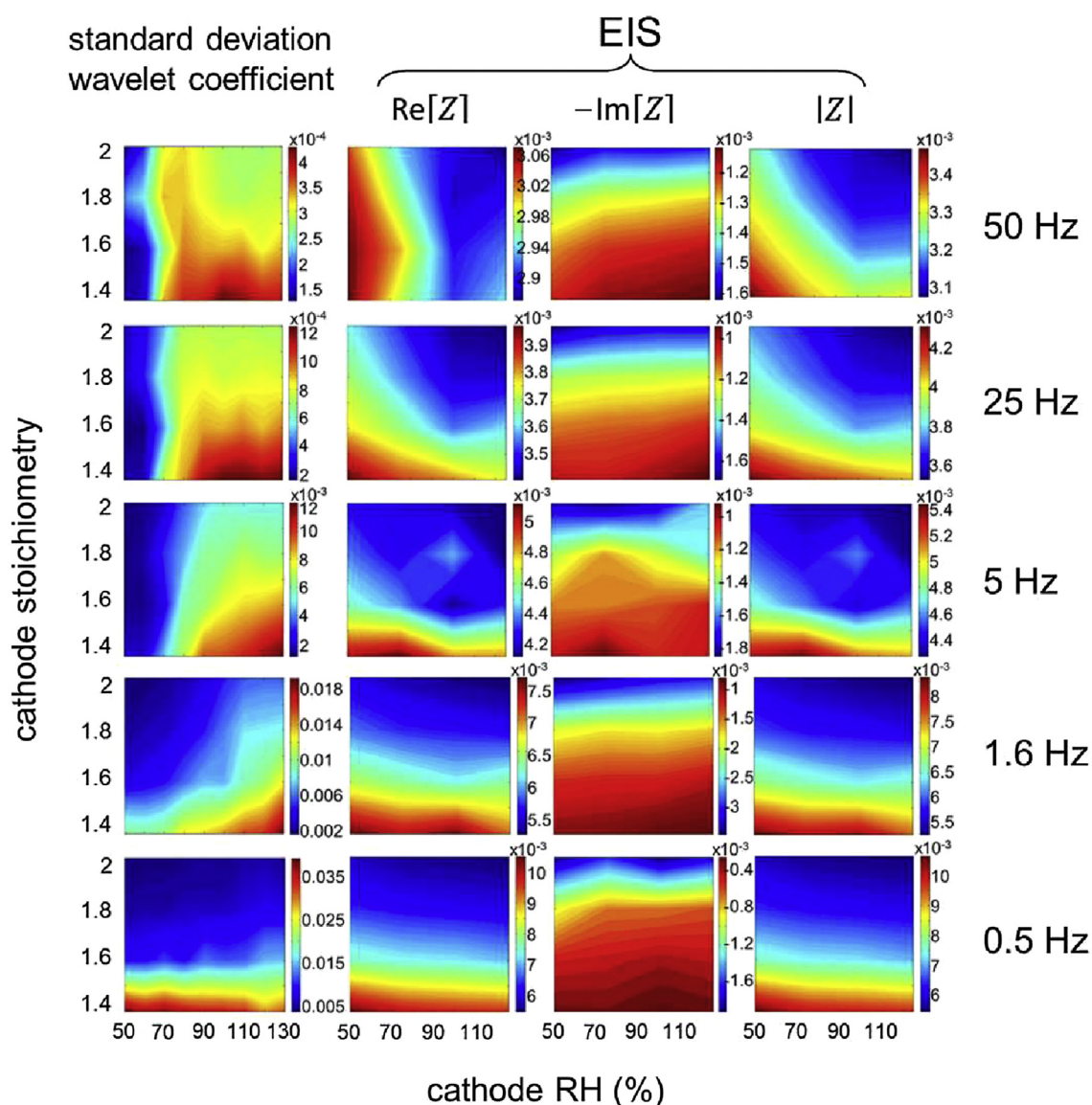


Fig. 9 – Comparison between the standard deviation of the wavelet coefficients and the EIS measurements.

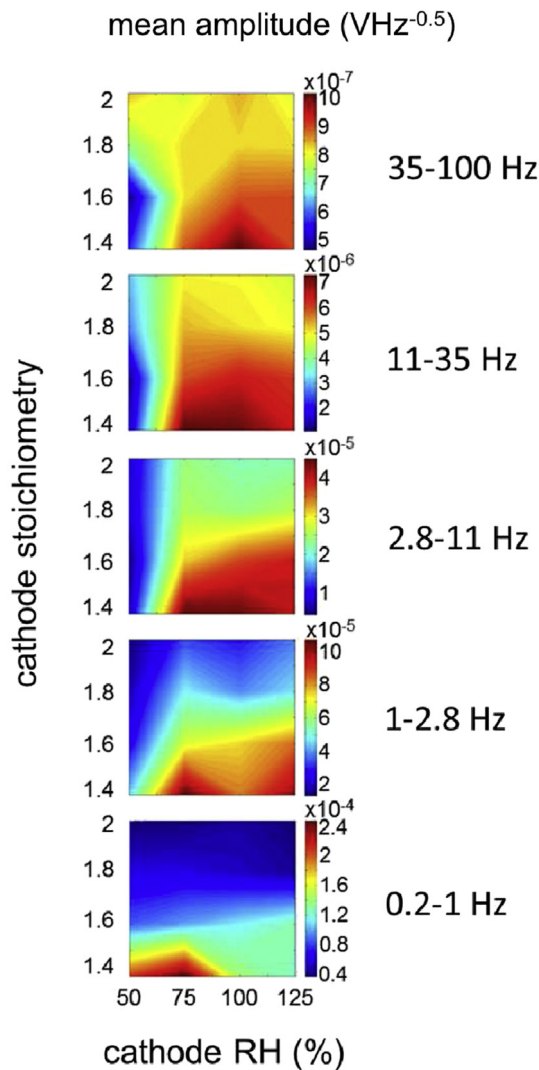


Fig. 10 – Average spectra amplitude for five frequency bands and different values of the cathode relative humidity and cathode stoichiometry.

the expected changes resulting from air stoichiometry (first order oxygen reduction kinetics [47] and oxygen and liquid water mass transfer [48]) and relative humidity (liquid water flooding [49], ionomer dehydration decreasing oxygen permeability [50]) variations. For the higher frequency characteristics of the oxygen reduction kinetics, the real impedance and the modulus of impedance decrease when the relative humidity increases. The greater ionomer permeability to oxygen and higher catalyst coverage by the swelled ionomer [51] increase both the oxygen concentration at the catalyst surface and real catalyst surface area. Both of these effects decrease the oxygen reduction impedance and modulus by respective decreases in overpotential (first order kinetics) and real current density. For the lower frequencies typical of oxygen mass transport, the real impedance and modulus values decrease when the stoichiometry increases. The greater average concentration across the cell leads to a larger average oxygen concentration difference between the

Table 1 – Ratio between highest and lowest values of the measured parameters' ranges.

Frequency or frequency range (Hz)	Standard deviation of wavelet coefficient (V Hz ^{-0.5})	Re[Z] (Ω)	Im[Z] (Ω)	z (Ω)	Mean amplitude (V Hz ^{-0.5})
50 or 35-100	2.7	1.1	1.3	1.1	2
25 or 11-35	6	1.1	1.6	1.2	3.5
5 or 2.8-11	6	1.2	1.8	1.2	4
1.6 or 1-2.8	9	1.4	3	1.5	5
0.5 or 0.2-1	7	1.7	4	1.7	6

flow field channel and the catalyst surface which promotes larger mass transfer rates and a smaller oxygen mass transfer impedance and modulus. The values of the imaginary part of the impedance decrease when the stoichiometry increases because they are linked to the real parts by the existence of a semi-circular loop assigned to mass transfer (Fig. 6, <10 Hz). As the radius of the loop decreases, both real and imaginary impedances for a given frequency also diminish.

Fig. 10 pertains to the STFT analysis with frequency window averaging. The mean amplitude values of the spectrum for the selected frequency bands are directly comparable to the EIS measurements and the standard deviation of the wavelet coefficients (Fig. 9) as they were obtained under the same conditions.

The mean amplitude of the spectrum correlates with the standard deviation of the wavelet coefficients. This is expected because the frequency bands are centered at the frequencies of the calculated wavelet coefficients.

It was mentioned in the introduction that both STFT and WT methods are equally suitable to analyze signals in real time. The sensitivity of each method is compared using the ratio between the highest and lowest values of the measured parameters' ranges used in Figs. 9 and 10 (Table 1). Table 1 reveals that the EIS is the least sensitive method, whereas the WT transform method is the most sensitive. Furthermore, the WT transform method yielded much larger coefficient values than the mean amplitudes derived using the STFT method. Therefore, the potential of the WT for fuel cell diagnosis is further explored in the next section.

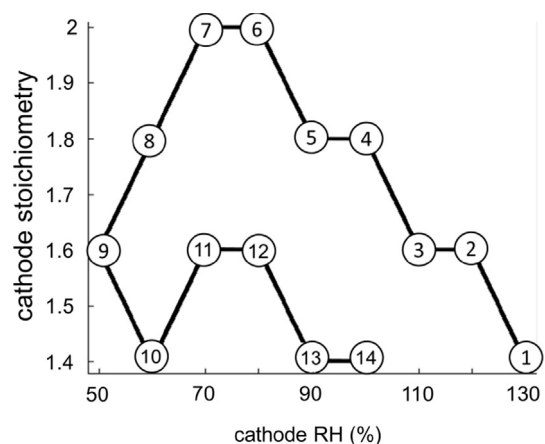


Fig. 11 – Cell states considered for the prediction method demonstration.

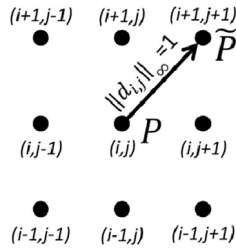


Fig. 12 – Chebyshev distance between states $\{i,j\}$ and $\{i^*=i+1, j^*=j+1\}$.

Robustness analysis of the diagnosis procedure

Measurements of the wavelet coefficient standard deviation, which corresponds to known values of the cell state, are used as a reference to estimate the cell's actual state. This statement implies that training will be necessary and will have to be demonstrated under dynamic conditions. Experiments need to be performed to estimate the standard deviations of the wavelet coefficient for an extensive set of known cell states. Additionally, constant current and steady state data are used here for concept demonstration rather than dynamic automotive conditions. The algorithm used to identify the state is based on a brute force search. Other options are feasible, e.g., grouping the states according to cell overvoltage levels or using classification methods based on neural networks [52–54].

The proposed procedure is suitable for real-time diagnosis if implemented with a digital signal processor [55–57].

Fuel cell state prediction method

The cell state is represented using two quantities: the air relative humidity and stoichiometry. These two quantities are the experimental factors. The levels of each factor are numbered using integer numbers. This allows designating the experimental points (i.e., the cell states) using a pair of integer numbers $\{i,j\}$. The first number indicates the air relative humidity level and the second number the air stoichiometry level. The set of all experimental points $\{i,j\}$ is designated as D .

The standard deviation of the m -th wavelet coefficient, $\sigma_w(m,N)$, is calculated as shown in Eq. (7). The standard deviation of the $\{i,j\}$ experimental point is represented as $\sigma_w(m,N)|_{\{i,j\}}$. In general, the number of experimental factors can be greater than two. In that case, the calculated standard

deviations are represented as $\sigma_w(m,N)|_{\{i,j,k,\dots\}}$, where $\{i,j,k,\dots\}$ is the experimental point.

The actual cell state is estimated as follows. The cell voltage is measured and the standard deviations, $\sigma_w(m,N)$, of the wavelet coefficients are calculated by applying Eq. (7). The actual cell state is estimated to be the experimental point $P = \{i,j,k,\dots\} \in D$ that minimizes the expression in Eq. (9).

$$\sum_{z=1}^M \left| \left(1 - \frac{\sigma_w(m_z, N)}{\sigma_w(m_z, N)|_{\{i,j,k,\dots\}}} \right) \right| \quad (9)$$

where M is the number of different wavelet functions used.

Method robustness

Fourteen of the 56 experimental points are shown in Fig. 11. They are represented as $P_1, \dots, P_{14} \in D$. The standard deviations that were calculated for these experimental points are represented as $\sigma_w(m,N)|_{P_1}, \dots, \sigma_w(m,N)|_{P_{14}}$. For each of these 14 states, the cell state identification is performed from data generated by adding random variations to the experimental standard deviation calculated for the state (i.e., $\sigma_w(m,N)|_{P_1}$ for P_1 , $\sigma_w(m,N)|_{P_2}$ for P_2 , etc.). These random variations are independent and uniformly distributed with a mean equal to 0 and a range equal to a percentage of the corresponding experimental standard deviation. The following seven percentages were used: 5, 10, 15, 20, 25, 30 and 35%.

The state corresponding to each of these generated values of the standard deviation is calculated by minimizing Eq. (9). The Chebyshev distance between this calculated state $\{i^*, j^*\}$ and the true state $\{i,j\}$ (i.e., the state used to generate the standard deviation value) is calculated from Eq. (10), as illustrated in Fig. 12 for a specific case.

$$||d_{i,j}||_{\infty} = \max \left\{ \sqrt{(i - i^*)^2}, \sqrt{(j - j^*)^2} \right\} \quad (10)$$

Table 2 defines 2 extreme regions. For a pre-determined mean Chebyshev distance of 0.05, states P7 and P8 were the most easily identifiable because the corresponding error exceeds 35%. These states have low relative humidity and high cathode stoichiometry. Conversely, states P1, P2, P10, P13 and P14, which have a low cathode stoichiometry, are the most difficult to identify because the corresponding error is relatively lower at 10–20%. These observations are consistent with an expected larger cell voltage standard deviation under mass transfer conditions, which are more prevalent at low stoichiometries and greater air relative humidities and current densities [45].

Table 2 – Mean Chebyshev distance between the estimated and true states.

Error	P1	P2	P3	P4	P5	P6	P7	P8	P9	P10	P11	P12	P13	P14
5%	0	0	0	0	0	0	0	0	0	0	0	0	0	0
10%	0	0	0	0	0	0	0	0	0	0.022	0	0	0.002	0.032
15%	0.010	0.009	0.001	0	0.001	0	0	0	0.001	0.117	0	0	0.072	0.165
20%	0.068	0.052	0.021	0.038	0.037	0.008	0	0	0.030	0.224	0	0.001	0.202	0.365
25%	0.141	0.110	0.076	0.143	0.107	0.053	0	0	0.109	0.277	0	0.013	0.297	0.483
30%	0.247	0.219	0.185	0.272	0.233	0.126	0	0	0.177	0.301	0	0.094	0.465	0.542
35%	0.343	0.332	0.284	0.461	0.370	0.242	0	0.001	0.234	0.349	0	0.210	0.641	0.619

Conclusions

The diagnosis of proton exchange membrane fuel cells was explored by comparing Fourier and wavelet transform analyses of cell voltage noise to electrochemical impedance data. The main conclusions are:

- The wavelet transform procedure is preferred because it is suitable for real-time analysis and yields a relatively greater sensitivity to operating condition changes (air stoichiometry and relative humidity).
- The changes in the wavelet coefficient standard deviations for selected noise frequencies are sufficient to reconstruct the original fuel cell operating conditions state.

Future work will consider the following development aspects:

- Assess the suitability of the wavelet transform analysis with an enlarged fuel cell operating conditions state space by adding other relevant parameters, such as air contaminants, and by using the entire range investigated here (air starvation). It is emphasized that failure modes that do not lead to permanent fuel cell degradation were initially considered to minimize resource use. From that standpoint, many air contaminants create reversible effects [58].
- Develop and demonstrate a real-time diagnostic algorithm under dynamic conditions and for a larger set of failure modes.

Acknowledgments

Work by M. A. Rubio and A. Urquia was supported by the Ministerio de Economía y Competitividad of Spain grant DPI2013-42941-R. The authors are also grateful to the United States Office of Naval Research for financial support of this project (award N00014-13-1-0463). The authors are indebted to the Hawaiian Electric Company for ongoing support to the operations of the Hawaii Sustainable Energy Research Facility.

REFERENCES

- [1] St-Pierre J. PEMFC in situ liquid-water-content monitoring status. *J Electrochem Soc* 2007;154:B724–31.
- [2] Liu Z, Yang L, Mao Z, Zhuge W, Zhang Y, Wang L. Behavior of PEMFC in starvation. *J Power Sources* 2006;157:166–76.
- [3] Stumper J, Campbell S, Wilkinson D, Johnson M, Davis M. In-situ methods for the determination of current distributions in PEM fuel cells. *Electrochim Acta* 1998;43:3773–83.
- [4] Hauer K-H, Potthast R, Wüster T, Stolten D. Magnetotomography – a new method for analysing fuel cell performance and quality. *J Power Sources* 2005;143:67–74.
- [5] Searson P, Dawson J. Analysis of electrochemical noise generated by corroding electrodes under open-circuit conditions. *J Electrochem Soc* 1988;135:1908–15.
- [6] Gabrielli C, Keddam M. Review of applications of impedance and noise analysis to uniform and localized corrosion. *Corrosion* 1992;48:794–811.
- [7] Legat A, Dolecek V. Corrosion monitoring system based on measurement and analysis of electrochemical noise. *Corrosion* 1995;51:295–300.
- [8] Roberge P, Beaudoin R. Voltage noise measurements on sealed lead-acid batteries. *J Power Sources* 1989;27:177–86.
- [9] Martinet S, Durand R, Ozil P, Leblanc P, Blanchard P. Application of electrochemical noise analysis to the study of batteries: state-of-charge determination and overcharge detection. *J Power Sources* 1999;83:83–93.
- [10] Baert D, Vervaet A. Small bandwidth measurement of the noise voltage of batteries. *J Power Sources* 2003;114:357–65.
- [11] Xiao H, Mansfeld F. Evaluation of coating degradation with electrochemical impedance spectroscopy and electrochemical noise analysis. *J Electrochem Soc* 1994;141:2332–7.
- [12] Mansfeld F, Lee C, Zhang G. Comparison of electrochemical impedance and noise data in frequency domain. *Electrochim Acta* 1998;43:435–8.
- [13] Greisiger H, Schauer T. On the interpretation of the electrochemical noise data for coating. *Prog Org Coat* 2000;39:31–6.
- [14] Tan Y, Xie Q, Huang J, Duan W, Ma M, Yao S. Study on glucose biofuel cells using an electrochemical noise device. *Electroanalysis* 2008;20:1599–606.
- [15] Legros B, Thivel P, Bultel Y, Nogueira R. First results on pemfc diagnosis by electrochemical noise. *Electrochem Commun* 2011;13:1514–6.
- [16] Giurgea S, Tirnovan R, Hissel D, Outbib R. An analysis of fluidic voltage statistical correlation for a diagnosis of PEM fuel cell flooding. *Int J Hydrogen Energy* 2013;38:4689–96.
- [17] Koshekov K, Klikushin Y, Kobenko V, Evdokimov Y, Demyanenko A. Fuel cell diagnostics using identification measurement theory. *J Fuel Cell Sci Technol* 2014;11:051003.
- [18] Benouioua D, Candusso D, Harel F, Oukhellou L. Fuel cell diagnosis method based on multifractal analysis of stack voltage signal. *Int J Hydrogen Energy* 2014;39:2236–45.
- [19] Steiner NY, Hissel D, Mootguy P, Candusso D. Non-intrusive diagnosis of polymer electrolyte fuel cells by wavelet packet transform. *Int J Hydrogen Energy* 2011;36:740–56.
- [20] Benouioua D, Candusso D, Harel F, Oukhellou L. PEMFC stack voltage singularity measurement and fault classification. *Int J Hydrogen Energy* 2014;39:21631–7.
- [21] Kim J, Tak Y. Implementation of discrete wavelet transform based discrimination and state-of-health diagnosis for a polymer electrolyte membrane fuel cell. *Int J Hydrogen Energy* 2014;39:10664–82.
- [22] Legros B, Thivel P, Bultel Y, Boinet M, Nogueira R. Electrochemical impedance and acoustic emission survey of water desorption in nafion membranes. *Electrochem Solid-State Lett* 2009;12:B116–8.
- [23] Legros B, Thivel P, Bultel Y, Boinet M, Nogueira R. Acoustic emission: towards a real-time diagnosis technique for proton exchange membrane fuel cell operation. *J Power Sources* 2010;195:8124–33.
- [24] Roy S, Orazem M. Analysis of flooding as a stochastic process in polymer electrolyte membrane (PEM) fuel cells by impedance techniques. *J Power Sources* 2008;184:212–9.
- [25] Claycomb J, Brazdeikis A, Le M, Yarbrough R, Miller GGJ. Nondestructive testing of PEM fuel cells. *IEEE Trans Appl Supercond* 2003;13:211–4.

- [26] Niroumand A, Mérida W, Eikerling M, Saif M. Pressure-voltage oscillations as a diagnostic tool for PEFC cathodes. *Electrochem Commun* 2010;12:122–4.
- [27] Niroumand A, Mérida W, Saif M. PEM fuel cell low flow FDI. *J Process Contr* 2011;21:602–12.
- [28] Rubio MA, Urquía A, Kuhn R, Dormido S. Electrochemical parameter estimation in operating proton exchange membrane fuel cells. *J Power Sources* 2008;183:118–25.
- [29] Mulder G, Ridder FD, Coenen P, Weyen D, Martens A. Evaluation of an on-site cell voltage monitor for fuel cell systems. *Int J Hydrogen Energy* 2008;33:5728–37.
- [30] Kiyimik M, Güler I, Dizibüyük A, Akin M. Comparison of STFT and wavelet transform methods in determining epileptic seizure activity in EEG signals for real-time application. *Comput Biol Med* 2005;35:603–13.
- [31] Zhang Y, Guo Z, Wang W, He S, Lee T, Loew M. A comparison of the wavelet and short-time fourier transforms for doppler spectral analysis. *Med Eng Phys* 2003;25:547–57.
- [32] Cooper K, Smith M. Electrical test methods for on-line fuel cell ohmic resistance measurement. *J Power Sources* 2006;160:1088–95.
- [33] Mathworks documentation. Fast fourier transform (FFT). URL <http://es.mathworks.com/help/matlab/ref/fft.html>.
- [34] Rao R, Bopardikar A. Wavelet transforms: introduction to theory and applications. Addison Wesley; 1998.
- [35] Benedetto JJ, Frazier M. Wavelets: mathematics and applications. CRC Press; 1994.
- [36] Orazem M, Tribollet B. Electrochemical impedance spectroscopy. John Wiley and Sons; 2008.
- [37] Hassibi A, Navid R, Dutton R, Lee TH. Comprehensive study of noise processes in electrode electrolyte interfaces. *J Appl Phys* 2004;96:1074–82.
- [38] Cheng Y, Luo J, Wilmott M. Spectral analysis of electrochemical noise with different transient shapes. *Electrochim Acta* 2000;45:1763–71.
- [39] Yan Q, Toghiani H, Causey H. Steady state and dynamic performance of proton exchange membrane fuel cells (PEMFCs) under various operating conditions and load changes. *J Power Sources* 2006;161:492–502.
- [40] Mathworks documentation. Scale to frequency (scal2frq). URL <http://es.mathworks.com/help/wavelet/ref/scal2frq.html>.
- [41] Zhai Y, Baturina O, Ramaker D, Farquhar E, St-Pierre J, Swider-Lyons K. Chlorobenzene poisoning and recovery of platinum-based cathodes in proton exchange membrane fuel cells. *J Phys Chem C* 2015;119:20328–38.
- [42] Schneidera IA, Kuhn H, Wokaun A, Scherer GG. Fast locally resolved electrochemical impedance spectroscopy in polymer electrolyte fuel cells. *J Electrochem Soc* 2005;152:A2092–103.
- [43] Nakamura S, Nishikawa H, Aoki T, Ogami Y. The diffusion overpotential increase and appearance of overlapping arcs on the nyquist plots in the low humidity temperature test conditions of polymer electrolyte fuel cell. *J Power Sources* 2009;186:278–85.
- [44] Taniguchi A, Akita T, Yasuda K, Miyazaki Y. Analysis of degradation in PEMFC caused by cell reversal during air starvation. *Int J Hydrogen Energy* 2008;33:2323–9.
- [45] St-Pierre J, Jia N. Successful demonstration of ballard PEMFCs for space shuttle applications. *J New Mater Electrochem Syst* 2002;5:263–71.
- [46] Zhai Y, Bethune K, Bender G, Rocheleau R. Analysis of the SO₂ contamination effect on the oxygen reduction reaction in PEMFCs by electrochemical impedance spectroscopy. *J Electrochem Soc* 2012;159:B524–30.
- [47] Zhdanov VP, Kasemo B. Kinetics of electrochemical O₂ reduction on Pt. *Electrochem Commun* 2006;8:1132–6.
- [48] Boyer C, Gamburzev S, Appleby AJ. Evaluation of methods to increase the oxygen partial pressure in PEM fuel cells. *J Appl Electrochem* 1999;29:1095–102.
- [49] Turhan A, Heller K, Brenizer J, Mench M. Quantification of liquid water accumulation and distribution in a polymer electrolyte fuel cell using neutron imaging. *J Power Sources* 2006;160:1195–203.
- [50] Broka K, Ekdunge P. Oxygen and hydrogen permeation properties and water uptake of Nafion 117 membrane and recast film for PEM fuel cell. *J Appl Electrochem* 1997;27:117–23.
- [51] Lindström RW, Kortsdotir K, Wesselmark M, Oyarce A, Lagergren C, Lindbergh G. Active area determination of porous Pt electrodes used in polymer electrolyte fuel cells: temperature and humidity effects. *J Electrochem Soc* 2010;157:B1795–801.
- [52] Übeyli ED. Combined neural network model employing wavelet coefficients for EEG signals classification. *Digit Signal Process* 2009;19:297–308.
- [53] Inan OT, Giovannrandi L, Kovacs GTA. Robust neural-network-based classification of premature ventricular contractions using wavelet transform and timing interval features. *IEEE Trans Biomed Eng* 2006;53:2507–15.
- [54] Mao PL, Aggarwal RK. A novel approach to the classification of the transient phenomena in power transformers using combined wavelet transform and neural network. *IEEE Trans Power Del* 2001;16:654–60.
- [55] Mota HO, Vasconcelos FH, da Silva RM. Real-time wavelet transform algorithms for the processing of continuous streams of data. In: *IEEE international workshop on intelligent signal processing*; 2005. p. 346–51.
- [56] Patil S, Abel E. Real time continuous wavelet transform implementation on a dsp processor. *J Med Eng Technol* 2009;33:223–31.
- [57] Hai-Chun Y. A TMS320C6416 DSP real time implementation of continuous wavelet filtering module. *Procedia Eng* 2011;23:665–70.
- [58] St-Pierre J, Zhai Y, Angelo MS. Effect of selected airborne contaminants on PEMFC performance. *J Electrochem Soc* 2014;161. F280–90 and 162 (2015) X7.